Review of Scientific Instruments

Time-resolved velocity and ion sound speed measurements from simultaneous bow shock imaging and inductive probe measurements

Cite as: Rev. Sci. Instrum. **93**, 103530 (2022); https://doi.org/10.1063/5.0098823
Submitted: 12 May 2022 • Accepted: 01 September 2022 • Published Online: 20 October 2022
Published open access through an agreement with Massachusetts Institute of Technology

R. Datta, D. R. Russell, I. Tang, et al.

Review of Scientific Instruments ARTICLE scitation.org/journal/rsi

Time-resolved velocity and ion sound speed measurements from simultaneous bow shock imaging and inductive probe measurements

Cite as: Rev. Sci. Instrum. 93, 103530 (2022); doi: 10.1063/5.0098823
Submitted: 12 May 2022 • Accepted: 1 September 2022 •
Published Online: 20 October 2022

R. Datta,[1] D. R. Russell,[2] I. Tang,[2] T. Clayson,[2] L. G. Suttle,[2] J. P. Chittenden,[2] S. V. Lebedev,[2] and J. D. Hare[1,a)]

AFFILIATIONS

[1] Plasma Science & Fusion Center, Massachusetts Institute of Technology, Cambridge, Massachusetts 02139, USA
[2] Blackett Laboratory, Imperial College London, London SW7 2BW, United Kingdom

Note: This paper is part of the Special Topic on Proceedings of the 24th Topical Conference on High-Temperature Plasma Diagnostics.
[a)]**Author to whom correspondence should be addressed:** jdhare@mit.edu

ABSTRACT

We present a technique to measure the time-resolved velocity and ion sound speed in magnetized, supersonic high-energy-density plasmas. We place an inductive ("b-dot") probe in a supersonic pulsed-power-driven plasma flow and measure the magnetic field advected by the plasma. As the magnetic Reynolds number is large ($R_M > 10$), the plasma flow advects a magnetic field proportional to the current at the load. This enables us to estimate the flow velocity as a function of time from the delay between the current at the load and the signal at the probe. The supersonic flow also generates a hydrodynamic bow shock around the probe, the structure of which depends on the upstream sonic Mach number. By imaging the shock around the probe with a Mach–Zehnder interferometer, we determine the upstream Mach number from the shock Mach angle, which we then use to determine the ion sound speed from the known upstream velocity. We use the sound speed to infer the value of $\bar{Z}T_e$, where $\bar{Z}$ is the average ionization and T_e is the electron temperature. We use this diagnostic to measure the time-resolved velocity and sound speed of a supersonic ($M_S \sim 8$), super-Alfvénic ($M_A \sim 2$) aluminum plasma generated during the ablation stage of an exploding wire array on the Magpie generator (1.4 MA, 250 ns). The velocity and $\bar{Z}T_e$ measurements agree well with the optical Thompson scattering measurements reported in the literature and with 3D resistive magnetohydrodynamic simulations in GORGON.

I. INTRODUCTION

To adequately diagnose laboratory plasma experiments, it is necessary to measure several plasma quantities within the finite lifetime of the generated plasma. As this often requires an extensive diagnostic suite, it can be advantageous if a single diagnostic can measure multiple quantities simultaneously.

In highly conducting plasmas with frozen-in magnetic flux, localized time-resolved measurements of a magnetic field can also provide information about the plasma velocity. The inductive ("b-dot") probe is one of the simplest magnetic diagnostics—a loop of wire that outputs a voltage due to time-varying magnetic flux. It provides a cost-efficient and effective alternative to more advanced diagnostic techniques, such as Faraday rotation[1] and proton radiography.[2,3] B-dot probes have been used extensively in magnetized high-energy-density (HED) plasmas. In laser-driven plasmas, which exhibit rapidly evolving Biermann-generated or externally imposed fields, multi-axis probes are used to reconstruct spatially and temporally resolved 3D magnetic fields.[4–7] Similarly, b-dot probes are routinely fielded in pulsed-power-driven plasmas to measure the ~1 to 10 T fields advected by the plasma flows.[8,9]

The magnetic Reynolds number $R_M = UL/\bar{\eta}$ represents the relative importance of the magnetic field advection over resistive

diffusion. Here, U is the plasma velocity, L is the characteristic length, and $\tilde{\eta}$ is the magnetic diffusivity. For large $R_M \gg 1$, advection dominates and the magnetic field becomes frozen into the flow. In magnetized plasmas with frozen-in flux, inductive probes can provide an estimate of the flow velocity[5,10]—a quantity typically measured using techniques such as optical Thompson scattering (OTS) and[11–13] Mach probes,[14] or from the Doppler shift of spectral lines.[15] B-dot measurements have previously been used to estimate the expansion velocity of laser-driven $R_M \sim 10^4$ plasma bubbles[5] and velocities in subsonic magnetic reconnection experiments.[10,16]

Flow velocity can be inferred by placing multiple probes along a velocity pathline and measuring the transit time of a magnetized fluid parcel between the probes. However, in situations where the first probe significantly perturbs the velocity or magnetic field, it may not be possible to position multiple probes along the same pathline. There are several ways to overcome this issue: (1) a single probe can be used, and its location can be varied between repeated shots,[5] (2) in the symmetric systems, probes can be positioned on different pathlines along the direction of symmetry, and (3) the magnetic field can be measured at the source, such as in the transmission line of a pulsed-power machine, and a probe can be placed in the flow to measure the advected field.

In addition to the flow velocity, inductive probes can also be used to estimate the Mach number and ion sound speed in supersonic plasmas. In a supersonic flow, the probe generates a 3D bow shock, as illustrated in Fig. 1. The geometry of a bow shock depends on the upstream Mach number.[8,17,18] In hydrodynamic shocks, the relevant Mach number is the sonic Mach number $M_S = U/C_S$; in magnetohydrodynamic (MHD) shocks, however, the shock geometry depends on both the sonic and the Alfvén Mach numbers, as well as on the orientation of the magnetic field.[17,19] Here, $C_S = \sqrt{\gamma \bar{Z} T_e/m_i}$ is the ion sound speed, which is a function of the adiabatic index of the plasma γ, the ionization $\bar{Z}$, the electron temperature T_e, and the ion mass m_i. The Alfvén Mach number $M_A = U/V_A$ is the ratio of the flow velocity to the Alfvén speed $V_A = B/\sqrt{\mu_0 \rho}$, which depends on the magnetic field B and density ρ.

At the resistive diffusion length $l_\eta = \tilde{\eta}/U$, the magnetic Reynolds number becomes $R_M = 1$, that is, the rates of advection and diffusion become comparable. Therefore, diffusion dominates for obstacles smaller than l_η, and the plasma and magnetic field decouple at the shock. For b-dot probes of diameter comparable to l_η, shocks around them will be hydrodynamic, and jumps in the magnetic field will be negligible.[20,21] By imaging the shock around a small b-dot probe, the upstream sonic Mach number M_S can be inferred, and we can further estimate the ion sound speed C_S if the flow velocity is known.

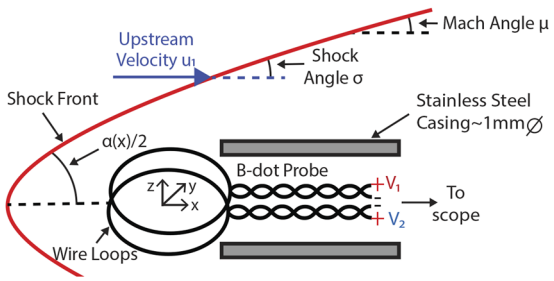

FIG. 1. B-dot probe with oppositely wound loops of enamel-coated copper wire, threaded through a thin-walled steel tube. The bow shock around the probe is represented by the red solid line.

In this paper, we estimate the temporally resolved velocity and the ion sound speed in a pulsed-power-driven magnetized HED plasma from simultaneous voltage measurements and imaging of bow shocks around small inductive probes. In comparison to previous experimental work in pulsed-power-driven plasmas, where inductive probes were used to measure the magnetic field upstream or downstream of shocks generated by planar[22] or cylindrical obstacles,[8] here, the probe itself serves as the obstacle. The small size of the probe compared to the resistive diffusion scale allows us to generate a 3D hydrodynamic shock, as described in the previous paragraph, whose structure is determined by the sonic Mach number, rather than the magnetosonic Mach number.[20] The experiments detailed here are also the first to provide the velocity and temperature measurements from inductive probe signals combined with bow shock imaging, in contrast to previous experiments that have used OTS for this purpose.

This paper is structured as follows: In Sec. II, we outline the methodology of velocity estimation from b-dot measurements. In Sec. III, we describe the diagnostic setup fielded on the Magpie pulsed-power machine. In Secs. IV and V, we present the velocity and sound speed measurements made using this diagnostic. Finally, in Sec. VI, we compare our measurements with 3D resistive MHD simulations and with OTS measurements reported in the literature.

II. VELOCITY MEASUREMENT WITH B-DOT PROBES

We want to determine how time-of-flight of the measured magnetic field relates to the flow velocity at the probe location. Consider a fluid parcel $x_p\ (x_0, t)$ which is at some initial position x_0 at time $t = 0$ in a magnetized high-R_M plasma with a 1D time-varying velocity field $u\ (x, t)$. The fluid parcel travels to a position $x_p\ (x_0, \tau) = x_0 + s$ after some time τ. Using probes positioned at $x = x_0$ and $x = x_0 + s$, we measure the transit time τ of the fluid parcel. The average speed $\bar{u}$ of the fluid parcel along its trajectory over the time period τ is $\bar{u} = s/\tau = (1/\tau)\int_0^\tau \dot{x}_p(x_0, t)\, dt$.

The expression within the integral is the Lagrangian velocity $\dot{x}_p(x_0, t)$ of the fluid parcel, which can be related to the Eulerian velocity field $u\ (x, t)$ using $\dot{x}_p(x_0, t) = u(x, t)|_{x=x_p(x_0,t)}$. For this calculation, we assume a simple Eulerian velocity field $u\ (x, t) = (U_0 + mx)e^{vt}$. We choose this velocity field as it allows for a simple analytical result and is a good approximation to the velocity field we simulate in the experiments described below, but the analysis outlined here can be performed for any arbitrary field. Substituting the given velocity field into the previous expression results in a first-order non-linear ordinary differential equation, the solution to which is the trajectory of the fluid parcel in the prescribed velocity field,

$$x_p(t) = -\frac{U_0}{m} + \frac{U_0 + mx_0}{m} \exp\left[\frac{m}{v}(e^{vt} - 1)\right]. \tag{1}$$

With the known trajectory, we can now calculate the average speed of the parcel,

$$\bar{u} = \frac{U_0 + mx_0}{m\tau}\left[\exp\left\{\frac{m}{\nu}\left(e^{\nu t} - 1\right)\right\} - 1\right]. \quad (2)$$

This is the quantity measured from the probe signals. In most applications, however, we are more interested in the instantaneous flow velocity, which is the Eulerian velocity. We can compare the average Lagrangian velocity described by Eq. (2) to the flow velocity at the probe location $x = x_0 + s$, where the Eulerian flow velocity is $u_s \equiv u\left(x_p(\tau), \tau\right)$. Taking the ratio $\bar{u}/u_s$, we calculate the extent to which the averaged Lagrangian velocity overestimates or underestimates the Eulerian velocity at the probe location. Furthermore, we are free to choose the position of the origin in this problem, so we set $x_0 = 0$, and the ratio $\bar{u}/u_s$ then simply becomes a function of the dimensionless quantities $m\tau$ and $\nu\tau$,

$$R(m\tau, \nu\tau) \equiv \frac{\bar{u}}{u_s} = \frac{e^{-\nu\tau}}{m\tau}\left[1 - \exp\left\{\frac{m\tau}{\nu\tau}\left(1 - e^{\nu\tau}\right)\right\}\right]. \quad (3)$$

The value of R depends on the spatial and temporal variation of the velocity $u\left(x, t\right)$ between the points $x_0 < x < (x_0 + s)$ over the transit time τ. The quantity $\bar{u}$ inferred from the probe measurements overestimates the flow velocity at the probe location, i.e., $R > 1$, when the velocity field decreases both spatially $(m\tau < 0)$ and temporally $(\nu\tau < 0)$, while it underestimates the flow velocity when the velocity field increases both spatially $(m\tau > 0)$ and temporally $(\nu\tau > 0)$. When ν and m have opposite signs, the value of R will depend on the relative magnitude of these terms. For spatially and temporally constant velocity $(\nu, m \to 0)$, or small transit times $(\tau \to 0)$, $\bar{u}$ becomes equal to the Eulerian velocity at the probe location $(R \to 1)$. This means that a smaller probe separation allows for a better estimate of the Eulerian velocity. Estimating the quantity R requires some prior knowledge of the variation of the velocity field $u\left(x, t\right)$, which may be informed from the simulations, previous experiments, or analytical models.

III. DIAGNOSTIC SETUP AND DEMONSTRATION ON MAGPIE

The inductive probe used in this demonstration consists of two counter-wound single-turn loops of enamel coated copper wire, threaded through an ~ 1 mm OD thin-walled steel tube (Fig. 1). The loops have diameters of ~ 0.5 mm and are coated with silver paint for electrostatic shielding. The voltage signal from each loop is attenuated using a voltage divider and recorded separately using an oscilloscope with a 1 ns digitization rate. The voltage $V_{1,2}$ across each loop can have two distinct contributions—one due to the time-varying magnetic flux $\dot{\Phi}$ through the loop and the other due to stray voltages V_S from the pulsed-power generator: $V_{1,2} = \pm\dot{\Phi} + V_S$. Having two counter-wound loops allows us to combine the signals $V = 0.5(V_1 - V_2) = \dot{B}A_{\text{eff}}$. and isolate the contribution of the time-varying magnetic flux, which is the product of the rate of change of the magnetic field $\dot{B}$, and the effective loop area A_{eff}.

We position the probe to measure the azimuthal magnetic field advected by the plasma generated during the ablation stage of a 16 mm tall, a 16 mm wide exploding wire array with 16 equally spaced 30 μm diameter aluminum wires (California Wire Company), as illustrated in Fig. 2. Exploding wire arrays are commonly-used plasma sources for laboratory-astrophysics applications, and generate radially-diverging outflows of magnetized collisional plasma.[1,8,9,20,22] The probe is positioned 5.55± 0.25 mm from the wires, with the loop normal along the magnetic field (i.e., in the y-direction). We use a coordinate system centered at the intersection of the obstacle axis and the array surface, with the magnetic field contained in the x–y plane. The Magpie generator (Imperial College London) drives a 1.4 MA peak current, 250 ns rise time current pulse through the load.[23] Ablation of the plasma from the wires generates hypersonic $(M_S \sim 8)$ and super-Alfvénic $(M_A \sim 2)$ outflows with frozen-in magnetic flux $(R_M \sim 20)$.[8,9] The resistive diffusion length is $l_\eta \sim 0.3$–0.6 mm, comparable to the probe diameter. We calculate l_η using characteristic values of $U \sim 60$ km s^{-1}, $n_e \sim 10^{18}$ cm^{-3}, and $T_e \sim 10$–15 eV.[9]

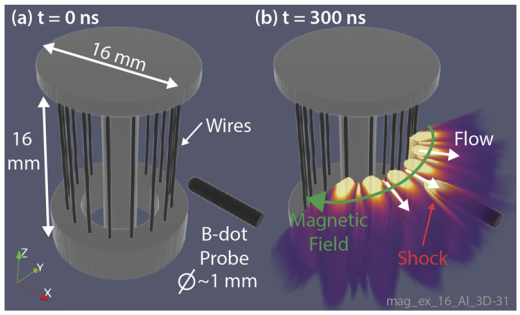

FIG. 2. (a) 3D representation of the experimental geometry, showing an exploding wire array with 16 equally spaced 30 μm Al wires. (b) Ablation of plasma from the wire array. Left and top half of the plasma has been clipped for clarity.

In addition to the probe in the flow, we place a second single-loop b-dot probe in a recess inside Magpie's magnetically insulated transmission line (MITL). This probe monitors the current delivered to the load, which in turn sets the driving magnetic field, a fraction of which is advected by the flow. For a 16 mm diameter array, driven by a $I_{\text{pk}} = 1.4$ MA current, the peak driving magnetic field is 35 T (calculated using Ampere's law), and the field measured in the plasma flow ~5 mm from the wires is typically ~10 T.[21] By measuring the time-of-flight between the driving and advected magnetic fields, we can estimate the flow velocity, as discussed in Sec. III.

To image the shock around the probe, we use a Mach–Zehnder interferometer with a 1053 nm Nd:glass laser (1 ns, 100 mJ). The interferometer provides a line-integrated (along the y-direction) view of the side-on (x–z) plane, with a ~2 cm diameter field-of-view. We combine the probe and reference beams at the CCD of a Canon EOS 500D DSLR camera, and calculate the line-integrated electron density from the fringe shift measured in the interferogram.[24,25]

We use the side-on line of sight to eliminate the effect of flux pile-up on the shock structure, which occurs when advected field lines accumulate and bend around an obstacle. The magnetic tension of the bent field lines opposes the ram pressure of the upstream flow, creating a wider shock than when there is no pile-up.[8,26] For 3D obstacles such as the inductive probe, pile-up increases the opening angle of the shock in the plane parallel to the magnetic field (the x–y plane), but not in the plane normal to the field (the side-on x–z plane).[8] This allows us to directly estimate the upstream Mach number from the side-on shock geometry.

We perform 3D resistive MHD simulations of the experimental geometry using GORGON to compare velocity and sound speed measurements with simulated values.[27,28] In this paper, we use a simple volumetric radiation-recombination model[29] with a constant multiplier to account for line radiation, and a local thermodynamic equilibrium (LTE) Thomas–Fermi equation-of-state[28] to determine the ionization level. The simulation domain is a cuboid with dimensions 60 × 60× 45 mm^3 and a resolution of 100 μm. The initial mass in the wires is distributed over 300 μm wide pre-expanded wire cores. The applied current pulse (1.4 MA, 250 ns) was determined by integrating the Rogowski signal monitoring the current in the cathode for a shot with a similar load.

IV. TIME-RESOLVED VELOCITY MEASUREMENTS

Figure 3(a) shows the unattenuated voltage signals from the oppositely wound loops of the b-dot probe in the flow, together with the signal from the probe near the MITL (henceforth, called the load probe). We combine the oppositely polarized signals from both loops to isolate the inductive signal [black curve in Fig. 3(a)]. The probe in the flow reproduces the shape and characteristic features of the signal at the load, showing that the magnetic field is frozen into the flow.

The features present in the signals (represented by the orange and black circles on the load and flow signals, respectively) are caused by voltage reflections due to impedance mismatches in the transmission lines of the pulsed-power machine.[23] These features are typically considered undesirable, as they represent inefficient signal transmission. However, the presence of these features allows us to measure time-of-flight of the plasma to the probe from the time delay between corresponding features on the two signals. From the known distance between the array and the flow probe, we estimate the time-resolved average velocity of the plasma between the wires and the probe over the transit time of the fluid parcel, as shown in Fig. 3(b).

Our simulation shows that the velocity field increases spatially with increasing distance from the array ($m > 0$) but decreases temporally ($v < 0$) (see Sec. II). From the simulated velocity field, we estimate $m \approx 2 \times 10^7$ s^{-1} and $v \approx -4.3 \times 10^6$ s^{-1}. The inductive probe measurements show that the mean transit time is $\tau \sim 78$ ns. This corresponds to a correction factor $R \sim 0.67$ [Eq. (3)], which indicates that the average velocity measured by the inductive probe is about 67% of the flow velocity at the probe location. The corrected velocity [green curve in Fig. 3(b)] estimates the Eulerian velocity at the probe location and ranges from ~170 km s^{-1} early in time to ~78 km s^{-1} later in time ($t \sim 300$ ns).

V. UPSTREAM MACH NUMBER AND ION SOUND SPEED

Figures 4(a) and 4(b) show the interferograms recorded before the start of the experiment and at t = 300 ns after the start of the current pulse, respectively. The line-integrated electron density, reconstructed from the distorted fringes, is shown in Fig. 4(c). A detached bow shock, which appears as a curved discontinuity in the fringes and the electron density, is visible in both the raw interferogram and the electron density map. The shock front appears washed-out in the electron density map because line-integrating through the bulk of the plasma obscures the intensity of the shock front. To enhance the visibility of the shock, we plot the gradient of the line-integrated electron density on a logarithmic scale [Fig. 4(d)].

The shock appears more prominent on the top of the probe in Figs. 4(b) and 4(c). This is because in the shot interferogram, the fringes shift in such a way that they become almost parallel to the shock front under the probe and, thus, appear relatively undistorted. The shock appears distinct on the other side, where the fringes are at an angle to the shock. Using a different imaging diagnostic, such

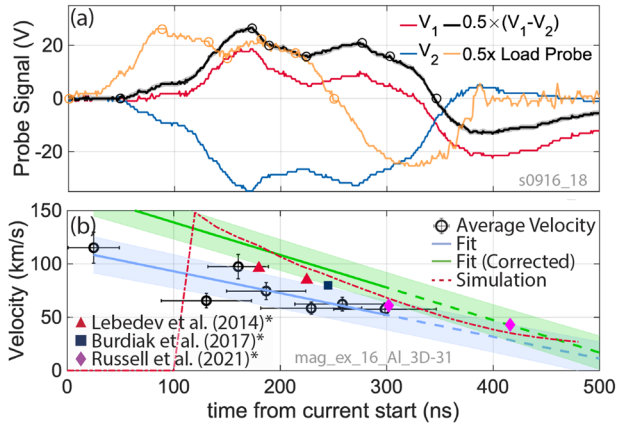

FIG. 3. (a) Voltage response of the inductive probe and the load probe. (b) Time-resolved average velocity measurements between the wires and probe location. Time error bars show a period over which velocity is averaged. Data marked with an asterisk represent OTS data. The green curve represents the corrected velocity using R = 0.67.

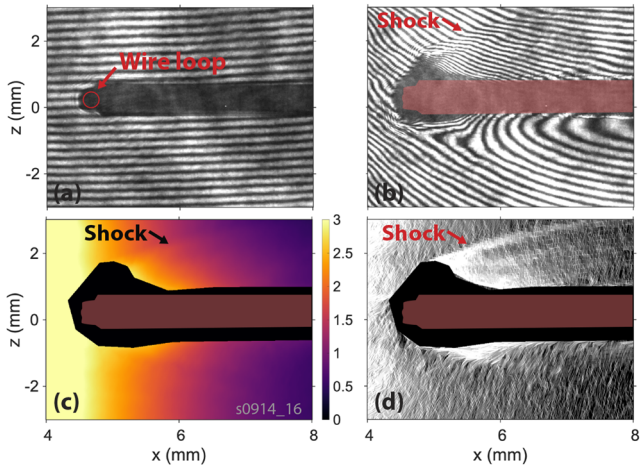

FIG. 4. (a) Side-on background interferogram recorded before current start. (b) Side-on raw interferogram at 300 ns after current start. The red shaded region represents the silhouette of the probe from the background interferogram. (c) Side-on line-integrated electron density map. (d) Enhanced image of the shock. Fine-scale structures seen here are artifacts of interpolation.

TABLE I. Experimentally measured quantities at probe location 300 ns after current start and comparison with the simulation and the literature.

	V (km s^{-1})	μ (deg)	M_S	C_S (km s^{-1})	$\bar{Z}T_e$ (eV)
Experiment	52 ± 14	7 ± 0.5	8.2 ± 0.6	6 ± 2	10 ± 6
Corrected	78 ± 14	7 ± 0.5	8.2 ± 0.6	9.5 ± 2	22 ± 9
Simulation	68	7	7 – 11	6 – 10	9 – 25
OTS[8,20,22]	61 ± 1	N/A	N/A	N/A	28 – 40

as shadowgraphy or Schlieren imaging with a symmetric stop, can eliminate this issue.

The shock angle $\sigma(x)$ in a bow shock is the angle between the upstream velocity vector $\mathbf{u_1}$ and the shock front (Fig. 1). The shock angle decreases continuously from 90° at the leading edge of the obstacle in a bow shock. Far away from the obstacle, where the shock is infinitesimally weak, the shock angle asymptotically approaches the Mach angle μ. We can relate the Mach angle to the upstream Mach number using the simple expression $\sin\mu = 1/M_S$.[17,30] From Fig. 4, we measure the Mach angle to be $\mu = 7.0° \pm 0.5°$, which corresponds to an upstream sonic Mach number of $M_S \sim 8.2 \pm 0.6$. Combining this information with the measured flow velocity, we estimate the ion sound speed C_S, as shown in Table I.

The ion sound speed C_S depends on the electron temperature T_e, the ionization $\bar{Z}$, and the adiabatic index γ of the plasma. If γ is known, we can use the estimated sound speed to infer the value of $\bar{Z}T_e$. In high-Z HED plasmas, internal energy and thermal pressure contributions due to Coulomb interactions, ionization, and excitation processes can make the adiabatic index of the plasma smaller than that of an ideal gas.[31] For the plasma in this experiment ($n_e \sim 1 \times 10^{18}$ cm^{-3}, $T_e \sim 10$ eV), we use a simple model to estimate $\gamma \approx 1.13$,[24,31] using which, we estimate $\bar{Z}T_e \sim 22 \pm 9$ eV (Table I).

VI. COMPARISON WITH THE SIMULATION AND THE LITERATURE

The velocity measured by the probe [blue curve in Fig. 3(b)] underestimates the simulated Eulerian velocity at the probe location, but applying a correction factor of $R \sim 0.67$ results in good agreement with the simulation. As seen in Table I, experimental estimates of the Mach angle, Mach number, and sound speed also agree well with simulated values.

The first velocity data point in Fig. 3(b), however, represents a discrepancy between the experiment and simulation. In the experiment, the plasma reaches the probe earlier than in the simulation. Wire arrays typically exhibit a ~50 ns dwell time before ablation begins, which means that it is unlikely that there is a plasma at the probe location at $t = 50$ ns after start of the current pulse. A magnetostatic Biot–Savart calculation of the vacuum magnetic field shows that the contribution of the vacuum field to the probe's voltage response is only ~20 mV at peak current, which is not large enough to explain the rising voltage at 50 ns. Further investigation is required to resolve the discrepancy in the plasma arrival time.

In Fig. 3(b), we also compare the flow velocity determined from inductive probe measurements with velocity measurements reported in the literature. These measurements are acquired using optical Thompson scattering (OTS) in experiments with aluminum exploding wire arrays of similar dimensions, also fielded on Magpie, and at roughly 5 mm from the wires.[8,20,22] OTS measures spatially localized flow velocity from the Doppler shift in the spectra of light scattered by the plasma.[11] The corrected flow velocity estimated from inductive probe measurements agrees, within experimental uncertainty, with OTS measurements reported in the literature.[8,20,22] The ion feature of OTS also allows for the measurement of $\bar{Z}T_e$ from the wavelength separation of the ion acoustic peaks in the scattered spectrum.[11] Values of $\bar{Z}T_e$ inferred from OTS in similar plasmas lie in the range $\bar{Z}T_e \sim 28 - 40$ eV.[8] This range is consistent with the values obtained by the corrected inductive probe technique reported herein ($ZT_e \sim 22 \pm 9$ eV).

VII. SUMMARY

We present a new experimental technique to infer the velocity and ion sound speed in supersonic magnetized pulsed-power-driven plasmas from simultaneous imaging and voltage measurements of inductive probes. By measuring the transit time of the plasma between two inductive probes, we calculate the average velocity of a magnetized fluid parcel along its trajectory. We show that the extent to which the measured velocity overestimates or underestimates the instantaneous flow velocity at the probe location depends on the temporal and spatial variation of the velocity field. In this demonstration, we use a Mach–Zehnder interferometer to image the shock; however, other imaging techniques, such as shadowgraphy or Schlieren imaging, where the intensity of the image is proportional to density gradients (such as at the shock front), may enhance the visibility of the shock. We estimate the Mach number of the upstream flow from the Mach angle of the imaged shock, and combining this information with the measured velocity allows us to estimate the ion sound speed, which agrees well with the prediction of our simulation and with OTS measurements reported in the literature.

ACKNOWLEDGMENTS

This work was funded by the NSF and NNSA under Grant No. PHY2108050 and supported by the DOE under Award Nos. DE-SC0020434, DE-NA0003764, DE-F03-02NA00057, DE-SC-000 1063, and DE-NA0003868 and the EPSRC under Grant No. EP/N0 13379/1. Simulations were performed on the Engaging cluster funded by Award No. DE-FG02-91-ER54109.

AUTHOR DECLARATIONS

Conflict of Interest

The authors do not have any conflict of interest to disclose.

Author Contributions

R. Datta: Formal analysis (equal); Investigation (equal); Visualization (equal); Writing – original draft (equal); Writing – review & editing (equal). **D. R. Russell**: Investigation (equal); Writing – review & editing (equal). **I. Tang**: Investigation (equal). **T. Clayson**: Investigation (equal). **L. G. Suttle**: Investigation (equal);

Writing – review & editing (equal). **J. P. Chittenden**: Software (equal); Supervision (equal). **S. V. Lebedev**: Conceptualization (equal); Funding acquisition (equal); Supervision (equal); Writing – review & editing (equal). **J. D. Hare**: Conceptualization (equal); Investigation (equal); Supervision (equal); Writing – review & editing (equal).

DATA AVAILABILITY

The data that support the findings of this study are available from the corresponding author upon reasonable request.

REFERENCES

[1] J. D. Hare *et al.*, Phys. Plasmas **25**, 055703 (2018).
[2] N. L. Kugland *et al.*, Rev. Sci. Instrum. **83**, 101301 (2012).
[3] G. Sutcliffe *et al.*, Rev. Sci. Instrum. **92**, 063524 (2021).
[4] E. T. Everson *et al.*, Rev. Sci. Instrum. **80**, 113505 (2009).
[5] J. J. Pilgram *et al.*, High Power Laser Sci. Eng. **10**, E13 (2022).
[6] J. M. Levesque *et al.*, Phys. Plasmas **29**, 012106 (2022).
[7] D. B. Schaeffer *et al.*, Phys. Plasmas **29**, 042901 (2022).
[8] G. C. Burdiak *et al.*, Phys. Plasmas **24**, 072713 (2017).
[9] L. G. Suttle *et al.*, Plasma Phys. Control. Fusion **62**, 014020 (2019).
[10] H. Ji *et al.*, Phys. Plasmas **6**, 1743 (1999).
[11] D. H. Froula *et al.*, Rev. Sci. Instrum. **77**, 10E522 (2006).
[12] M. J. Rosenberg *et al.*, Phys. Rev. E **86**, 101301 (2012).
[13] L. G. Suttle *et al.*, Rev. Sci. Instrum. **92**, 033542 (2021).
[14] I. H. Hutchinson, *Principles of Plasma Diagnostics* (Cambridge University Press, 2002).
[15] S. Suckewer *et al.*, Phys. Rev. Lett. **43**, 207 (1979).
[16] M. Yamada *et al.*, Phys. Plasmas **4**, 1936 (1997).
[17] J. R. Spreiter and A. Y. Alksne, Rev. Geophys. **7**, 11, https://doi.org/10.1029/rg007i001p00011 (1969).
[18] J. D. Anderson, *Fundamentals of Aerodynamics* (McGraw-Hill, 2001).
[19] J. P. Goedbloed *et al.*, *Advanced Magnetohydrodynamics* (Cambridge University Press, 2010).
[20] D. R. Russell *et al.*, arXiv:2201.09039 (2022)
[21] R. Datta *et al.*, arXiv:2208.04535 (2022).
[22] S. V. Lebedev *et al.*, Phys. Plasmas **21**, 056305 (2014).
[23] I. H. Mitchell *et al.*, Rev. Sci. Instrum. **67**, 1533 (1996).
[24] G. F. Swadling *et al.*, Phys. Plasmas **20**, 022705 (2013).
[25] J. D. Hare *et al.*, Plasma Phys. Control. Fusion **61**, 085012 (2019).
[26] L. J. Dursi and C. Pfrommer, Astrophys. J. **677**, 993 (2008).
[27] J. P. Chittenden *et al.*, Phys. Plasmas **11**, 1118 (2004).
[28] A. Ciardi *et al.*, Phys. Plasmas **14**, 056501 (2007).
[29] A. S. Richardson, "NRL plasma formulary" (US Naval Research Laboratory, 2019).
[30] P. K. Kundu *et al.*, *Fluid Mechanics*, 5th ed. (Academic Press, 2012).
[31] R. Drake, *High-Energy-Density Physics* (Springer, 2013).